

Photocurrent interference spectroscopy of solids and characterization of semiconductor solar-cell materials

Cite as: J. Appl. Phys. **135**, 243101 (2024); doi: [10.1063/5.0207057](https://doi.org/10.1063/5.0207057)

Submitted: 6 March 2024 · Accepted: 31 May 2024 ·

Published Online: 25 June 2024



Yoshihiro Ogawa,^{1,a)} Hirokazu Tahara,^{2,3,a),b)} and Yoshihiko Kanemitsu^{3,a)}

AFFILIATIONS

¹Graduate School of Education, Joetsu University of Education, Joetsu, Niigata 943-8512, Japan

²The Hakubi Center for Advanced Research, Kyoto University, Kyoto 606-8501, Japan

³Institute for Chemical Research, Kyoto University, Uji, Kyoto 611-0011, Japan

^{a)}Authors to whom correspondence should be addressed: ogawa@juen.ac.jp; tahara-hirokazu-cf@ynu.ac.jp; and kanemitsu@scl.kyoto-u.ac.jp

^{b)}Present address: Department of Physics, Graduate School of Engineering Science, Yokohama National University, Yokohama 240-8501, Japan.

ABSTRACT

Photocurrent measurements are widely used to study the intrinsic optoelectronic properties of semiconductors, such as photocarrier generation efficiency and carrier mobility, as well as evaluate the performance of optoelectronic devices, such as solar cells and photodetectors. Interferometric spectroscopy precisely measures optical properties and gathers optical spectra information on semiconductors. Consequently, photocurrent-based interferometric measurements, with high signal-to-noise ratios, high resolution, and broad frequency bandwidths, can probe the energy distributions of low-density defects and impurities and investigate charge transport in materials and devices. Here, we demonstrate that photocurrent interference spectroscopy reveals the intrinsic properties of solar-cell materials: bulk crystals of GaAs and halide perovskite, and thin films of halide perovskite and quantum dot. We show that homodyne interference spectroscopy of photocurrent can monitor low-density localized states in semiconductors and that it can be used in combination with other spectroscopy techniques, such as photoluminescence measurements, to provide a deep understanding of photocurrent generation processes. Furthermore, we show that heterodyne interference spectroscopy of photocurrent can be used to investigate the frequency dependence of material parameters, such as the dielectric constant, absorption coefficient, and reflectance. As an application, we used interference spectroscopy of photocurrent to show the impact of multiexcitons on the photoabsorption and photocarrier generation processes in quantum dot solar cells. Finally, we used it to reveal the distinctive spectral characteristics at the band edge of a halide perovskite, which is considered to be an exceptional solar-cell material with high energy conversion efficiency.

© 2024 Author(s). All article content, except where otherwise noted, is licensed under a Creative Commons Attribution (CC BY) license (<https://creativecommons.org/licenses/by/4.0/>). <https://doi.org/10.1063/5.0207057>

I. INTRODUCTION

Photocurrent measurements can be used to investigate the current generated by light irradiating a material.^{1–3} Here, the photons excite electron–hole pairs in a material, which in turn generate a current when they reach the electrodes. The magnitude of this current varies depending on the intensity and wavelength of the excitation light, meaning that it can be used to study material attributes, such as photocarrier generation efficiency and carrier

mobility. Together with other optical measurement methods, photocurrent spectroscopy can be used to advance studies on semiconductor materials. It can precisely determine fundamental physical properties, such as the bandgap energy and photoelectric properties of a material.^{4–7} Furthermore, photocurrent measurements are vital for characterizing devices that convert light energy into electrical energy, such as optical sensors and solar cells. In particular, they aid in assessing the photoabsorption characteristics and spectral

29 June 2024 17:17:24

responses of photovoltaic materials, offering insights into the ideal wavelength range and methods for enhancing photoabsorption efficiency. Additionally, these measurements can be used to identify factors influencing device quality, such as defects, impurities, and electrical conduction properties inside the sample. Photocurrent spectroscopy is indispensable for examining localized levels in semiconductor materials that affect the performance and durability of light-emitting diodes and solar cells. Consequently, achieving high sensitivity in photocurrent spectroscopy is crucial.

As a way of increasing the sensitivity of photocurrent measurements, we have focused on interferometric spectroscopy. This technique can provide information on small localized levels and tail states undetectable with conventional measurement methods. There are two types of interferometry: homodyne and heterodyne. Homodyne interference involves two overlapping light waves of the same frequency.⁸ Typically, a laser beam is split into two beams on different optical paths and then the beams are realigned coaxially in both time and space, resulting in interference. This interference changes the light intensity, by either amplifying or attenuating it depending on the interference conditions. The interferometric waveform provides spectral information about a sample. Homodyne interferometry often uses a phase-locked technique to stabilize the interferometer.

On the other hand, heterodyne interference employs two light waves of different frequencies to create interference. This method requires two light sources having different frequencies, referred to as the reference wave and the signal wave. The reference wave, with a stable frequency, interferes with the signal wave, resulting in a beat. Heterodyne interference is insensitive to noise light because it uses lock-in detection of the beat signal, and thus, it enables more sensitive and accurate measurements than homodyne interference. However, it has a disadvantage of complicating the optical system.

These spectroscopic measurement methods based on interference have found widespread use as highly precise ways of measuring the optical characteristics and spectral information of materials. Homodyne interference, with its relatively straightforward optical setup, enables stable measurements, while heterodyne interference enables a high signal-to-noise-ratio and high-sensitivity measurements. Using photocurrent as a probe in optical interference measurements allows for precise evaluations of spectral information, identifications of defects and impurities, and analysis of electrical conduction characteristics of solar-cell materials and devices. Additionally, it has high resolution by taking long time sweeps of the interferometric waveform.

Photocurrent measurement techniques have advanced considerably in the time and frequency domains. Within the time domain, a number of techniques for measuring fast electronic responses have been developed.^{9–11} Concurrently, measurement techniques within the frequency (energy) domain have been extensively investigated. On the other hand, gaining an understanding of the authentic response of solar cells necessitates explorations beyond the conventional photocurrent measurement techniques based on monochromatic light irradiation; it requires methods based on broadband light irradiation. Hence, there is a need for a photocurrent spectrum measurement method that uses a broad band of light frequencies and has high energy resolution. In this Review article, we discuss a methodology for measuring

photocurrent spectra that utilizes interferometric spectroscopy. Our experimental demonstrations focused on GaAs, a prominent material for photo-to-current conversion, on quantum dots, where carrier multiplication processes via multiexcitons enhance the photon-to-electron conversion efficiency, and on lead-halide perovskites, which have shown potential for solar-cell technology. Although there is a method to measure absorption spectra using a Fourier transform infrared spectrometer with photocurrent as a probe,¹² we show that the novel phenomena, such as cooperative enhancement effect in quantum dots^{13,14} and coherent effect in lead-halide perovskites,¹⁵ can be measured using an ultrashort laser pulse in our method.

II. METHODS AND DISCUSSION

A. Homodyne interference spectroscopy of photocurrent

Homodyne interferometry is a spectroscopic technique for measuring the amplitude and phase of a signal wave by using two-wave mixing with another wave of the same frequency. The reference wave is called the local oscillator, and its amplitude and phase should be stabilized for measuring the amplitude and phase of the signal wave precisely. However, the stabilization in the optical frequency is often disturbed by fluctuations of the experimental system. In particular, fluctuations in the optical path length make it hard to use femtosecond pulses to investigate photocurrent generation mechanisms on a very short time scale. To solve this problem, we developed a method that measures the photocurrent spectrum by using a phase-locked pulse pair instead of a local oscillator.¹⁶

Figure 1(a) shows the experimental setup for phase-locked photocurrent beat spectroscopy. An excitation-pulse pair is generated by using a Mach-Zehnder interferometer. Part of the excitation-pulse pair is reflected by a beam splitter, and the interference intensity of that part is monitored after it goes through a monochromator. The homodyne interference signals are measured by scanning the time interval between the pulses constituting the pair. Here, a feedback loop with a piezoelectric actuator is used to keep the relative phase between the pulses in-phase or out-of-phase. By using this method, we can determine the resonance frequency ω_{res} of the photocurrent peak from the lock frequency ω_{lock} and beat frequency ω_{beat} : $\omega_{\text{res}} = \omega_{\text{lock}} - \omega_{\text{beat}}$. In other words, we can measure the optical frequency ω_{res} through the downconversion procedure to the beat frequency ω_{beat} . A direct measurement of the optical frequency ω_{res} is easily disturbed by fluctuations of the experimental system, while the downconversion procedure avoids this fluctuation problem and can measure the photocurrent spectrum precisely.

We performed photocurrent beat spectroscopy on bulk GaAs. Figure 1(b) shows the experimental photocurrent signals under in-phase and out-of-phase locking conditions at room temperature. The lock frequency ω_{lock} was set to the center wavelength of the excitation pulse. The oscillation signal corresponding to the beat frequency $\omega_{\text{beat}} = \omega_{\text{lock}} - \omega_{\text{res}}$ was clearly observed in the photocurrent measurement. We determined the resonance energy $\hbar\omega_{\text{res}} = 1394$ meV from $\hbar\omega_{\text{beat}} = 47$ meV and $\hbar\omega_{\text{lock}} = 1441$ meV. Since this resonance energy is lower than the band-edge energy by

29 June 2024 17:17:24

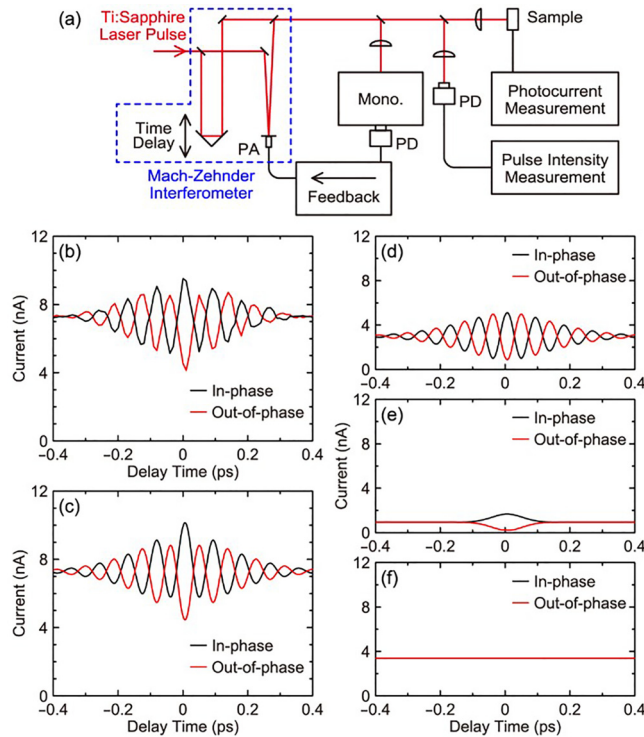


FIG. 1. (a) Experimental setup of phase-locked photocurrent beat spectroscopy. PD, photodetector; PA, piezoelectric actuator; and Mono., monochromator. An excitation-pulse pair is generated by using a Mach-Zehnder interferometer (blue dashed line). (b) Experimental and (c) calculated photocurrent signals from bulk GaAs at room temperature. Calculated photocurrent components of (d) band-acceptor transition, (e) band-to-band transition, and (f) background current. Adapted with permission from H. Tahara and Y. Kanemitsu, *Phys. Rev. B* **90**, 245203 (2014). Copyright 2014 American Physical Society.¹⁶

26 meV, this peak corresponds to the band-acceptor transition.^{16,17} In addition to the band-acceptor transition, the experimental oscillation profile involves two different photocurrent signals originating the band-to-band transition and the background current. As shown in Fig. 1(c), the oscillation profile was well reproduced by the summation of three photocurrent signals originating the band-acceptor transition [Fig. 1(d)], the band-to-band transition [Fig. 1(e)], and the background current [Fig. 1(f)]. This means that the oscillation profile exactly reflects information on the different photocurrent generation sources and that photocurrent beat spectroscopy is a powerful tool for acquiring this information.

Fourier transforming the photocurrent oscillation signals is useful for analyzing the details of multiple sources. In particular, it can clarify the relation between the ionization of acceptor levels and the generated photocurrent. Here, to observe the details of the thermal ionization and photocurrent generation processes, we performed photocurrent beat spectroscopy on GaAs at cryogenic temperatures.¹⁸ The obtained interferences involved multiple oscillation signals with different frequencies, which means that multiple photocurrent sources existed. The Fourier spectra of the

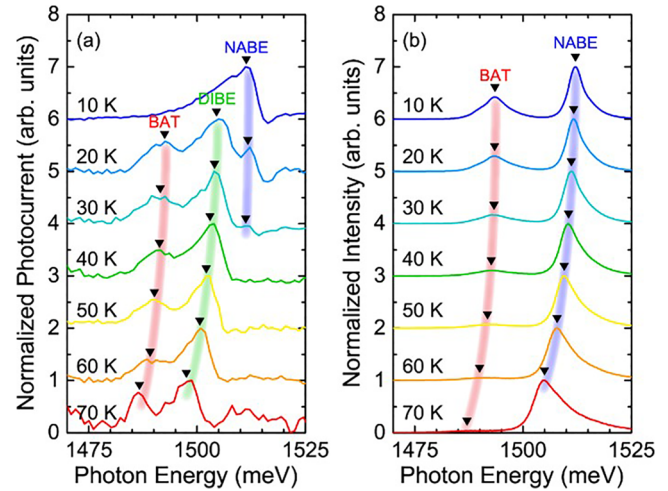


FIG. 2. (a) Fourier transform spectra of photocurrent beat signals and (b) photoluminescence spectra of bulk GaAs at different cryogenic temperatures. NABE, neutral-acceptor bound exciton; DIBE, defect-induced bound exciton; and BAT, band-to-acceptor transition. Adapted with permission from H. Tahara and Y. Kanemitsu, *Appl. Phys. Express* **9**, 032403 (2016). Copyright 2016 The Japan Society of Applied Physics.¹⁸

oscillation signals, shown in Fig. 2(a), have three peaks corresponding to neutral-acceptor bound exciton, defect-induced bound exciton, and band-to-acceptor transition. Since the defect-induced bound exciton is generated by partially ionized acceptors, these peaks are related to the ionization process of the acceptor levels. The neutral level at 1511 meV is the dominant peak at 10 K, while the partially ionized level (1498 meV) and the fully ionized level (1487 meV) become dominant at 70 K. This temperature-dependent change in the relative intensity ratio indicates that the photocurrent generation processes are directly governed by thermal ionization of the acceptor levels. Note that the peak structure in the photocurrent spectra is different from that of the photoluminescence (PL) spectra shown in Fig. 2(b), where the neutral level is the strongest PL peak regardless of temperature. Upon comparing the photocurrent and PL spectra, we can conclude that electron-hole radiative recombination is likely to occur at the neutral level, which reduces the amount of photocurrent, and that radiative recombination is suppressed at the ionized level causing a large increase in photocurrent.

The above demonstration shows that photocurrent beat spectroscopy is sensitive to weak photocurrent sources, and that photocurrent generation processes can be analyzed in detail with the assistance of different spectroscopic techniques, such as PL measurements. To further demonstrate the usefulness of this method, we used it to examine another solar-cell material: the halide perovskite MAPbI₃ (MA = CH₃NH₃).¹⁹ MAPbI₃ is an excellent solar-cell material possessing high solar-energy conversion efficiency. We clarified that the defect states in MAPbI₃ are shallow enough to be deactivated at room temperature, which explains the defect tolerance of MAPbI₃; i.e., photogenerated carriers of MAPbI₃ are hardly trapped by the defects.

29 June 2024 17:17:24

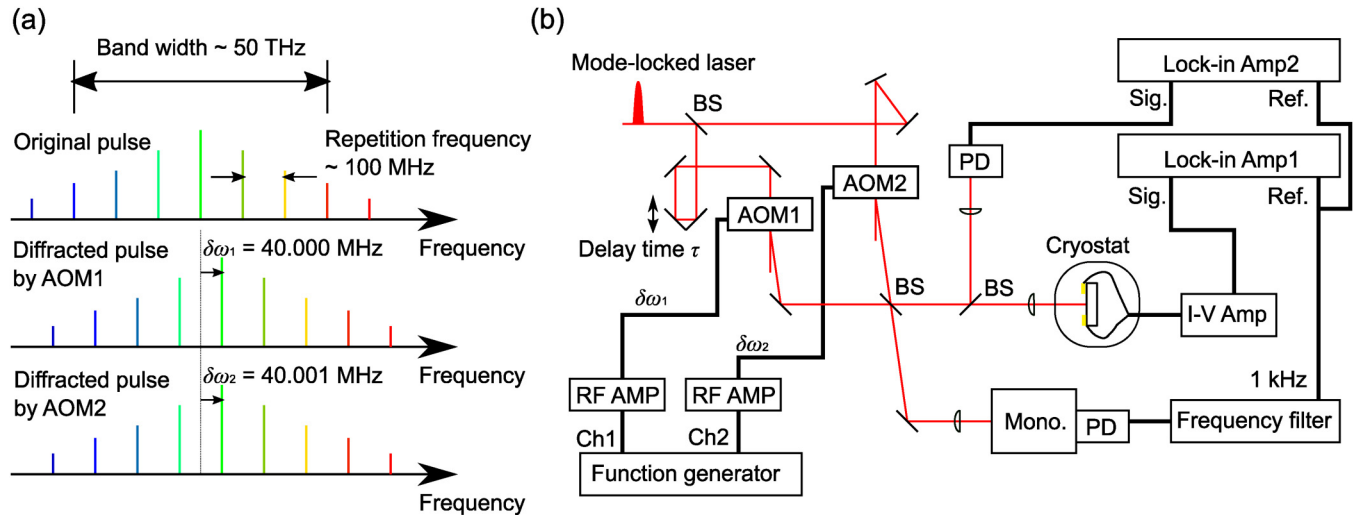


FIG. 3. (a) Spectra of an original mode-locked pulse and pulses diffracted by acousto-optic modulators. (b) Experimental setup. AOM, acousto-optic modulator; PD, photodetector; Mono, monochromator; BS, beam splitter; RF AMP, RF amplifier; I-V Amp, current amplifier; and Lock-in Amp, lock-in amplifier.

B. Heterodyne interference spectroscopy of photocurrent

Heterodyne interferometry combines a signal wave and a reference wave and measures their difference-frequency beats. This technique was first developed for studies in the radio frequency range, but it is also be used in studies involving high-frequency, coherent laser light. In particular, whereas the high frequency of visible light makes it difficult to measure its phase, the amplitude and phase of beats can be easily measured by adjusting the frequency difference between the signal and the reference lights from the kHz range to the MHz range. If the amplitude and phase of the reference light are known, the amplitude and phase of the signal light can be demodulated from the amplitude and phase of the beat.

Here, we used an acousto-optic modulator (AOM) to generate reference and signal lights with slightly different frequencies. When a radio frequency (RF) sound wave is applied to the optical crystal (crystalline quartz, tellurium dioxide, etc.) inside the AOM, the crystal acts as a diffraction grating. The incident beam is diffracted in a direction that conserves the momentum of the optical beam and the sound wave. The power of the diffracted beam depends on the RF power, so the light intensity can be controlled and modulated at a rate in excess of the speed of a mechanical shutter.

When an ultra-short laser pulse is used as the incident light, one might assume that the modulation by the AOM is negligible because the bandwidth of the pulse (~ 50 THz) is much larger than that of the RF (~ 40 MHz). However, in a mode-locked laser, a comb structure emerges in the spectrum, in which the spacing between the comb frequencies is equal to the laser's repetition frequency (~ 100 MHz). As shown in Fig. 3(a), a pair of light pulses frequencies shifted by the difference frequency (~ 1 kHz) of the

two AOMs' RFs can be generated by splitting the laser pulse into two with a beam splitter and frequency modulating each beam with an AOM. Since the spectral width of a single comb is sufficiently smaller than 1 kHz, interference beats at 1 kHz can be detected when the optical pulse pairs temporally and spatially overlap.

In the experimental system depicted in Fig. 3(b), a mode-locked laser pulse is injected into a Mach-Zehnder interferometer to produce an optical pulse pair. One arm of the interferometer includes an X stage to vary the time interval τ between the pulse pairs. An AOM is inserted in each arm of the interferometer to modulate the frequency of the pulse pairs by $\delta\omega_1 = 40.000$ MHz and $\delta\omega_2 = 40.001$ MHz. When a portion of the optical pulse pair is fed into the spectrometer and the specific wavelength component is extracted, the time width of the pulse is broadened. Consequently, even if the time interval τ of the pulse pair exceeds the pulse width, interference occurs between the pulse pairs, resulting in a beat. This beat signal serves as a reference signal for the lock-in amplifier. Photocarriers are generated upon irradiating the sample with the optical pulse pair. The photocarriers undergo through an energy relaxation process as they travel to the gold electrodes deposited on the sample surface, and upon reaching the electrodes, they appear as an electric current. The separation between the electrodes is $100\mu\text{m}$, and the current is converted to a voltage by an I-V amplifier. This signal constitutes the input to the lock-in amplifier. Simultaneously, the signal of the excitation pulse is measured by using a photodetector (PD) to detect a portion of the light pulse pair before they irradiate the sample. When the time interval τ of the optical pulse pair is scanned, an oscillatory waveform emerges in the interferogram that corresponds to the frequency disparity between the reference light and the

29 June 2024 17:17:24

electronic state. By analyzing the frequency and amplitude of this interferogram (via a Fourier transform), it becomes possible to determine the electronic state of the sample.

Information about the spectrum can be obtained by Fourier transforming the measured interferogram $\tilde{C}(\tau)$,²⁰

$$\begin{aligned}\tilde{C}(\omega) &= \int_{-\infty}^{\infty} \tilde{C}(\tau) e^{i\omega\tau} d\tau \\ &= \sum_n \mu_{ng}^2 E^2(\omega_{ng}) \exp \left[i\phi_{12}(\omega') - i\phi_{12}(\omega_{ng}) \right] \\ &\quad \times 2\pi\delta(\omega + \omega' - \omega_{ng}),\end{aligned}$$

where μ_{ng} is the electric dipole moment, ω_{ng} is the angular frequency of the electronic states of the sample $|n\rangle$, and ω' is the angular frequency of the monochromator. The phase term in square brackets is due to the asymmetry of the interferometer, but it can be removed by taking the absolute value. In addition, since a delta function, which is included in the summation, the electric dipole moment and the incident electric field spectrum are decoupled,

$$|\tilde{C}(\omega)| = 2\text{Im}[\tilde{\chi}(\omega + \omega')] \times E^2(\omega + \omega'),$$

where $\text{Im}[\tilde{\chi}(\omega)]$ is the imaginary part of the dielectric susceptibility,

$$\tilde{\chi}(\omega) = \sum_n \mu_{ng}^2 \left\{ \frac{1}{\omega_{ng} - \omega} + i\pi\delta(\omega - \omega_{ng}) \right\}.$$

Next, let us consider the Fourier transform of the interferogram in the regions where τ is positive and negative. The integral transform in the positive domain is

$$\begin{aligned}\tilde{C}_0^\infty(\omega) &= \int_0^\infty \tilde{C}(\tau) e^{i\omega\tau} d\tau \\ &= \sum_n \mu_{ng}^2 E^2(\omega_{ng}) \exp \left[i\phi_{12}(\omega') - i\phi_{12}(\omega_{ng}) \right] \\ &\quad \times \left\{ \frac{-i}{\omega_{ng} - \omega - \omega'} + \pi\delta(\omega + \omega' - \omega_{ng}) \right\}.\end{aligned}$$

The integral transformation in the negative domain $\tilde{C}_{-\infty}^0(\omega)$ is obtained by changing $-i$ to $+i$ in the first term of the braces in the above equation. Therefore, by taking the absolute value of the difference between $\tilde{C}_0^\infty(\omega)$ and $\tilde{C}_{-\infty}^0(\omega)$, we obtain the following equation:

$$\begin{aligned}|\tilde{C}_0^\infty(\omega) - \tilde{C}_{-\infty}^0(\omega)| &= 2 \sum_n \mu_{ng}^2 \frac{1}{\omega_{ng} - \omega - \omega'} E^2(\omega_{ng}) \\ &\approx 2\text{Re}[\tilde{\chi}(\omega + \omega')] \times E^2(\omega + \omega').\end{aligned}$$

$\text{Re}[\tilde{\chi}(\omega)]$ represents the real part of the dielectric susceptibility. An approximation is employed on the second line wherein the

spectrum of the excitation pulse is assumed to be sufficiently broad compared with the spectrum of the electronic response we are interested in. The spectrum of the excitation pulse, denoted as $E^2(\omega + \omega')$, can be derived by Fourier transforming the interferogram captured by the PD [refer to Fig. 3(b)]. Note that the frequency dependence of the PD can be corrected with known response function data.

To assess the accuracy of heterodyne interference spectroscopy, we performed experiments on a standard photoelectric conversion material, bulk GaAs. In particular, we performed interference spectroscopy measurements on photocurrent in GaAs by using the experimental system shown in Fig. 3(b), which included a mode-locked Ti:sapphire laser (KMLabs Ti:sapphire oscillator kit, operating at a wavelength of 800 nm, a repetition rate of 80 MHz, and a pulse width of 20 fs) as the pump source. The sample was cooled to 9 K in a cryostat. The wavelength of the monochromator was set to 809.0 nm.

Figures 4(a) and 4(b) show the interferogram of the photocurrent in GaAs and that of the excitation pulse captured by the PD placed in front of the sample. When the first pulse irradiated the GaAs, an electronic polarization is generated within the material. Because the lifetime of the polarization is longer than the temporal width of the optical pulse, the polarization persists even after the optical pulse disappears. As shown above, the dielectric susceptibility spectrum of GaAs can be derived through an integral transformation of the interferogram of the GaAs and excitation-pulse pairs [as illustrated in Fig. 4(c)]. By performing an integral transformation of the interferogram with the horizontal axis units in picoseconds (ps), a spectrum is obtained with a horizontal axis in terahertz (THz). The 0-THz point on the spectrum corresponds to the energy that corresponds to the wavelength of the monochromator, thereby enabling the units of the horizontal axis in Fig. 4(c) to be converted to energy (eV).

The methodology of the study described above does not allow for direct determination of the absolute value of the dielectric susceptibility $\tilde{\chi}(\omega)$. Consequently, we transformed $\tilde{\chi}(\omega)$ into the dielectric function $\tilde{\epsilon}(\omega)$ by utilizing the value of the dielectric function of GaAs in the literature²¹ and the relation $\tilde{\epsilon}(\omega) = \epsilon_0(1 + \tilde{\chi}(\omega))$. Subsequently, by employing the relations $n(\omega)^2 = (\sqrt{\tilde{\epsilon}'^2 + \tilde{\epsilon}''^2} + \tilde{\epsilon}')/2\epsilon_0$ and $\kappa(\omega)^2 = (\sqrt{\tilde{\epsilon}'^2 + \tilde{\epsilon}''^2} - \tilde{\epsilon}')/2\epsilon_0$ [where $\tilde{\epsilon}(\omega) = \tilde{\epsilon}'(\omega) + i\tilde{\epsilon}''(\omega)$], the refractive index $n(\omega)$ and the extinction coefficient $\kappa(\omega)$ could be computed. As shown in Fig. 4(d), although the refractive index remains nearly constant at 3.6, a distinctive kink structure is discernible around the bandgap energy E_g (1.519 eV) of GaAs. The extinction coefficient shows that there are absorptions at higher energies above E_g . Notably, the peak at 1.515 eV is due to exciton absorption.

The absorption coefficient $\alpha(\omega)$ and reflection $R(\omega)$ were derived from the refractive index $n(\omega)$ and the extinction coefficient $\kappa(\omega)$ by using the equations $\alpha(\omega) = 2\omega\kappa/n$ and $R(\omega) = |(n + i\kappa - 1)/(n + i\kappa + 1)|^2$ [as depicted in Figs. 4(e) and 4(f)]. Conventional photocurrent measurements were conducted to compare the absorption coefficient obtained via heterodyne interference spectroscopy with other experimental values. The same mode-locked laser utilized in the heterodyne interference spectroscopy measurements served as the light source. The pulsed light

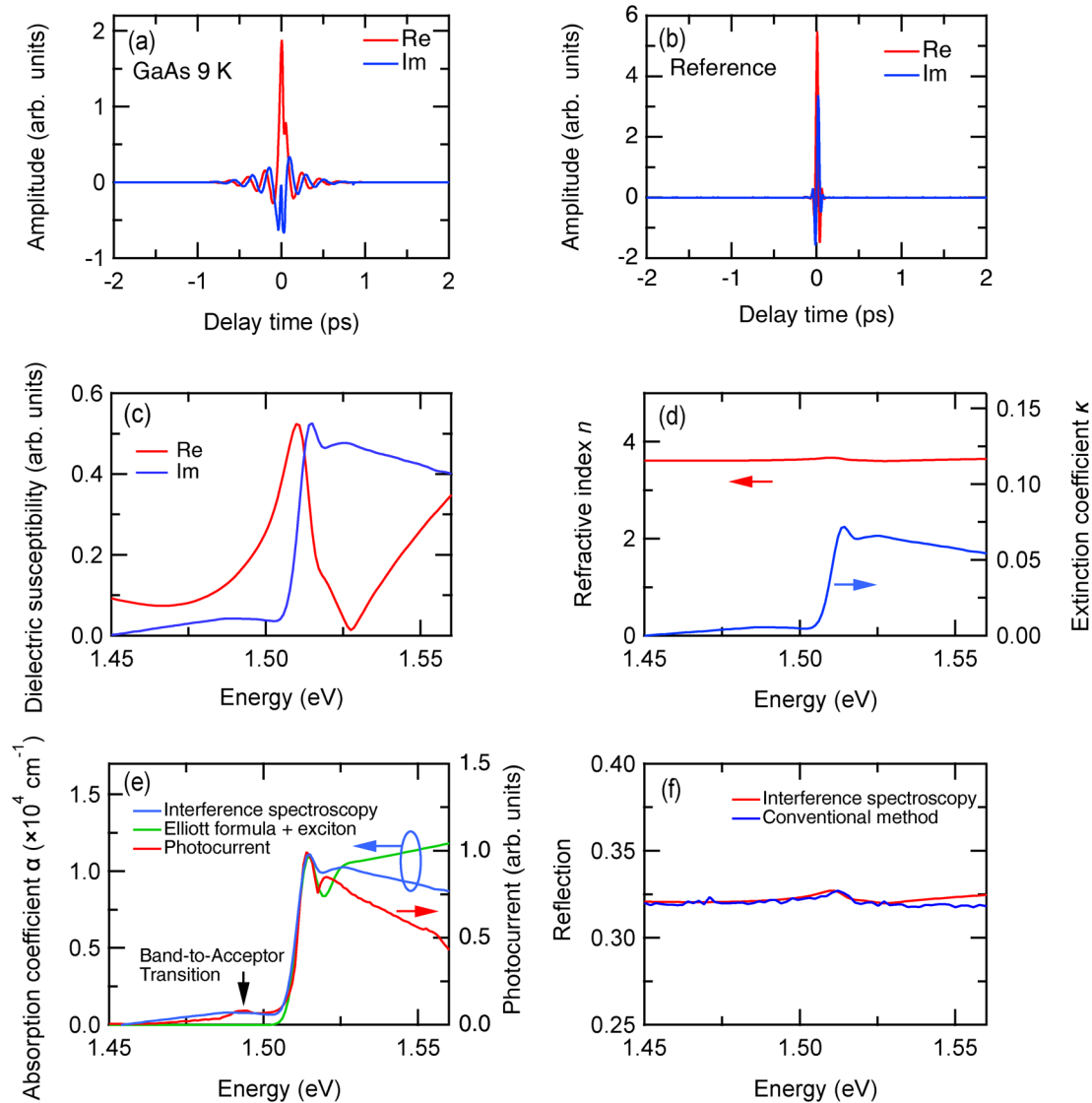


FIG. 4. Interferograms of (a) GaAs at 9 K and (b) excitation-pulse pair. The Re (Im) component represents the in-phase (90° -phase-shifted) component of the photocurrent signal with respect to the reference signal as measured by the lock-in amplifier. (c) Dielectric susceptibility obtained by performing an integral transformation on the interferograms. (d) Refractive index and extinction coefficient calculated from dielectric susceptibility. (e) Absorption coefficient obtained by interference spectroscopy, experimentally obtained photocurrent, and absorption coefficient calculated from the Elliott formula incorporating exciton effects. (f) Reflection obtained by interference spectroscopy and a conventional experimental method using a halogen lamp and a monochromator.

emitted by this source was spectrally resolved using a monochromator and then irradiated a sample cooled to 9 K. Notably, the photocurrent spectrum and the absorption spectrum were very similar at energies below the exciton absorption, encompassing the band-to-acceptor transition.¹⁸ Moreover, in the energy range beyond the exciton absorption, while there exists a quantitative discrepancy between the photocurrent spectrum and the absorption spectrum, both display a decrease in the intensity with increasing energy.

We used the Elliott formula²² to compute the absorption coefficient from the literature values²³ for E_g of 1.519 eV and an exciton binding energy of 4.9 meV of bulk GaAs at 9 K. Moreover, we used a Gaussian function to model the excitonic absorption line and phenomenologically introduced the linewidth as a fitting parameter. The calculated results are presented in Fig. 4(e). In general, the absorption coefficient increases as the density of states increases at energies higher than E_g .²⁴ However, Fig. 4(e) reveals that the absorption and photocurrent spectra acquired via heterodyne

interference spectroscopy exhibit a decline in intensity at higher energy levels. This observation suggests a potential decrease in efficiency of detecting hot carriers generated through optical absorption on the higher energy side. Such a decline is presumably due to the reduction in population caused by radiative recombination and thermal relaxation preceding the energy relaxation of hot carriers.¹

The reflection data acquired through heterodyne interference spectroscopy measurements were compared with the reflection data obtained through conventional reflectance measurements using a halogen lamp and a monochromator. The reflectance was calculated as the ratio between the intensities light reflected by the sample cooled to 9 K and light reflected by a metal mirror. As illustrated in Fig. 4(f), there is a noticeable correspondence between these reflections in the energy range below the exciton absorption.

We can address the disparities between the absorption and reflection data acquired through conventional means and the data obtained through heterodyne interference spectroscopy, particularly in the energy range beyond the exciton absorption. In heterodyne interference spectroscopy, the derivation of the dielectric susceptibility relies on the integral transformation of the interferogram. This transformation assumes that the spectrum width of the excitation pulse significantly exceeds that of the electronic response of interest. While this approximation holds for exciton absorption lines and band-to-acceptor transitions, it falters in the higher energy region of the band. Here, the spectral width of the excitation pulse becomes narrower than the spectral width of the response, rendering the approximation unsuitable. Consequently, the observed discrepancies manifest themselves in an energy range beyond the exciton absorption. Achieving an accurate determination of the spectrum encompassing the band's higher energy domain via heterodyne interference spectroscopy will necessitate the use of an ultra-short pulse laser endowed with a broader bandwidth. Nevertheless, the experiment managed to obtain the spectra within approximately 60 meV on the low-energy side of the exciton absorption line.

III. APPLICATION TO SOLAR-CELL MATERIALS

A. Homodyne interference spectroscopy of quantum dots

Homodyne interference spectroscopy is a powerful technique for analyzing solar-cell materials. We used it to measure the initial photoabsorption processes of quantum dots (QDs). QDs are potential next-generation solar-cell materials in which carrier multiplication processes arising from multiexcitons enhance the photon-to-electron conversion efficiency.^{25–29} However, the enhancement ratio is not strong enough to make full use of multiexcitons in practical applications. A detailed understanding of the photophysical processes of multiexcitons is, thus, required for improving the performance of QD solar cells.

Here, we investigated the initial photoabsorption processes and multiexciton behavior in PbS QD solar cells by using homodyne interference spectroscopy.^{13,14,30} The samples had a layered structure [Fig. 5(a)] in which the ZnO layer transported electrons and the MoO_x layer transported holes. The experimental setup is shown in Fig. 5(b). The center wavelength of the excitation pulse was set to 1038 nm, which corresponds to the exciton resonance of

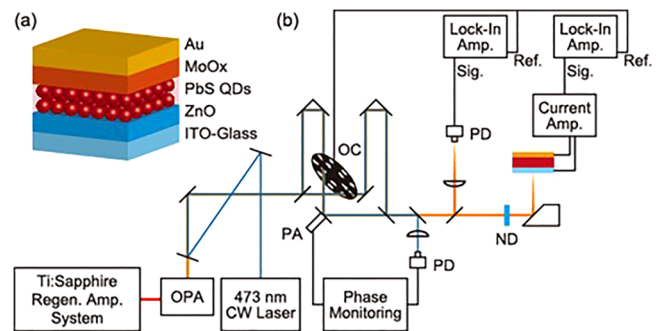


FIG. 5. (a) Schematic diagram of a QD solar cell used in the study. (b) Experimental setup of homodyne interference spectroscopy. The photocurrent signals from a QD solar cell were detected after they went through a current amplifier and a lock-in-amplifier. OPA, optical parametric amplifier; OC, optical chopper; PA, piezoelectric actuator; PD, photodetector; and ND, neutral density filter.

the QDs. An excitation-pulse pair was used in this system, similarly to the case of homodyne interference spectroscopy described in Sec. II. Note that the experiment described in Sec. II used a downconversion procedure to measure a photocurrent peak in the optical-frequency domain. In contrast, a direct measurement of optical-frequency interference is required to analyze multiexcitons in detail, because they produce multiple frequency signals higher than that of the fundamental excitation pulse.³¹ In order to directly measure the interference with high-resolution sampling, we used a 473-nm continuous-wave laser for monitoring the excitation-pulse interference. The interference patterns were measured by scanning a piezoelectric actuator in the optical path. At the same time, the interference patterns of the 473-nm laser were measured. Since the wavelength of the monitoring laser (473 nm) was shorter than the wavelength of the excitation pulse (1038 nm), oscillation signals with higher frequencies than the fundamental excitation frequency were detectable in the interference patterns.

The photocurrent interference patterns are shown in Figs. 6(a) and 6(b) for different excitation fluences. A single sinusoidal curve appeared in the case of the weak excitation [Fig. 6(a)]. This curve corresponds to the response from single excitons. In contrast, a multi-peaked interference pattern appeared in the case of the strong excitation [Fig. 6(b)]. The multi-peaked pattern indicates that the interference is composed of harmonic signals with $n\omega$ oscillations [Fig. 6(c)], i.e., the contributions from harmonic quantum coherent signals.^{31,32} Here, n is an integer and ω is the resonance frequency of single excitons. We analyzed the interference patterns by decomposing the signals into $n\omega$ oscillations. The obtained amplitudes A_n for $n\omega$ oscillations are plotted as black solid circles in Figs. 6(d)–6(g). The amplitude of the ω -oscillation signal [Fig. 6(d)] shows a saturation tendency corresponding to the probability of generating single excitons. This saturation tendency is described by $A_{s,1}(1 - \exp(-\langle N \rangle))$ with the saturated amplitude $A_{s,1}$ and the average number of absorbed photons per QD $\langle N \rangle$. The amplitudes of the higher-order oscillations ($n\omega$ -oscillation signals

29 June 2024 17:17:24

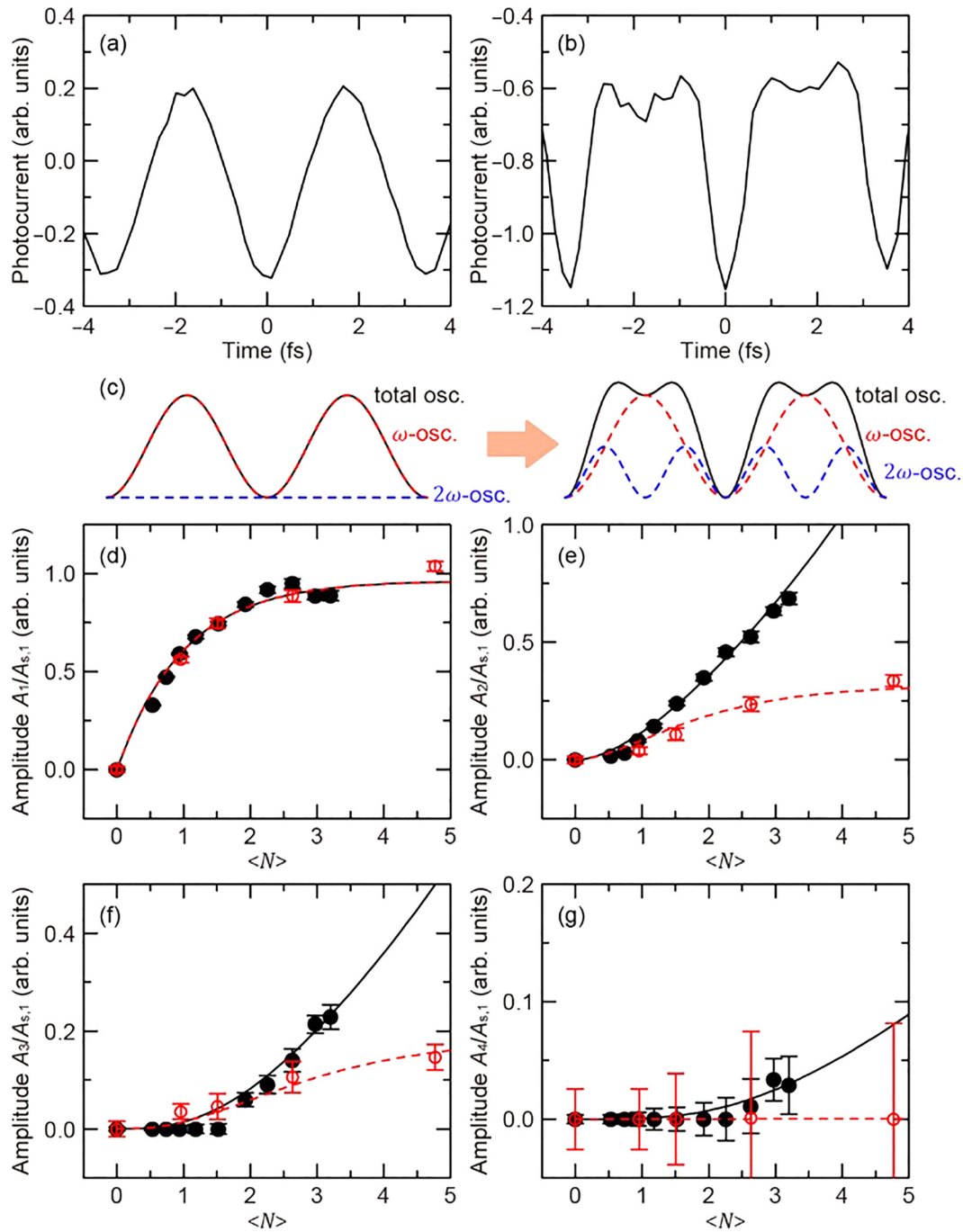


FIG. 6. Photocurrent interference signals for excitation photon fluences of (a) 0.35×10^{15} and (b) 2.09×10^{15} photons/cm². (c) Schematic interference patterns for (left) weak to (right) strong excitations. Amplitudes of (d) single-, (e) double-, (f) triple-, and (g) quadruple-oscillation signals for coupled (black solid circles) and isolated (red open circles) QDs are plotted as a function of the average number of absorbed photons. The amplitudes are normalized by the saturated amplitudes. The calculated results for coupled (isolated) QDs are shown as black solid (red dashed) curves. The data on coupled and isolated QDs are taken from Refs. 13 and 31, respectively. Adapted with permission from Tahara *et al.*, Phys. Rev. B **104**, L241405 (2021). Copyright 2021 Author(s), published by the American Physical Society, licensed under a Creative Commons Attribution 4.0 International License.¹³ Adapted with permission from Tahara *et al.*, Phys. Rev. Lett. **119**, 247401 (2017). Copyright 2017 Author(s), published by the American Physical Society, licensed under a Creative Commons Attribution 4.0 International License.³¹

for $n \geq 2$) show increasing tendencies with excitation fluence. These tendencies were not observed in the responses of the QD solution (red open circles). Therefore, we concluded that the increasing tendencies are caused by cooperative processes through the inter-QD couplings.^{13,14} We calculated the excitation fluence dependence of the harmonic oscillations by assuming that the multiexcitons arise from the inter-QD coupling. The black solid curves in Figs. 6(d)–6(g) are the calculated results, and they also show increasing tendencies. Thus, we clarified that the multiexcitons via the inter-QD coupling cooperatively enhance the photocurrent signals with higher oscillation frequencies in microscopic photoabsorption processes. Since the high-frequency oscillation relates to internal upconversion of photon energy, the quantum cooperative properties provide deep insights that can be used to improve the conversion efficiency of solar cells.

B. Heterodyne interference spectroscopy of lead-halide perovskites

Here, we used MAPbBr₃ single crystals (MA = CH₃NH₃) prepared with the inverse temperature crystallization method.³³ By using single crystals several millimeters in size, rather than thin films, we were able to minimize the effects of surfaces and interfaces. Whereas it is difficult to measure the absorption spectrum at the band edge in bulk crystals, we could use photocurrent as a probe. Although the luminescence from the single crystals at low temperatures contained complex components originating from impurities and defects, we could use photocurrent to accurately evaluate the band-edge and free exciton structure.¹⁵

The excitation light was produced by a regenerative amplifier pumped by a mode-locked Ti:sapphire laser (Coherent RegA, wavelength 800 nm, repetition frequency 200 kHz, pulse width 200 fs). Super-continuum light in the visible region was obtained by illuminating a sapphire substrate with this excitation light. As shown in Fig. 3(b), a Mach-Zehnder interferometer was used to generate a pair of light pulses from the super-continuum light. The sample was cooled in a cryostat, and the temperature was varied from 6.5 to 250 K.

Figure 7(a) shows the interferogram of the photocurrent of the MAPbBr₃ single crystal at 160 K. The wavelength of the reference light was 585.94 nm (2.116 eV), which was longer than E_g of the MAPbBr₃ single crystal and selected to be in the transparent region. The interferogram shows an oscillatory structure at about 16–22 fs that is due to the energy difference between the reference light and E_g . The interferogram of the excitation-pulse pair was obtained by measuring the light pulse pair before irradiation of the sample with a photodiode [Fig. 7(b)]. To remove the effects of long-term power fluctuations of the excitation laser, two lock-in amplifiers were used to simultaneously measure the interference waveforms of the photocurrent and the excitation-pulse pair.

We obtained the spectra of the real and imaginary parts of the dielectric susceptibility by performing an integral transformation on the interferogram.¹⁵ Then, we converted the dielectric susceptibility into the refractive index n and the extinction coefficient κ by using the literature values of the dielectric function of MAPbBr₃ single crystals [Fig. 7(c)].³⁴ We used super-continuum light in the

visible region to measure the bandwidth and found it to be about 0.4 eV. Note that the experiment on GaAs described in Sec. II B used a Ti:sapphire laser with a pulse width of 20 fs, so in that case, the bandwidth was only about 0.1 eV [refer to Fig. 4(c)].

The spectra converted from the reflective index n and the extinction coefficient κ to the absorption coefficient α are shown in Fig. 7(d). The photocurrent spectrum measured by dispersing the super-continuum light with a monochromator is also shown. E_0 in the figure denotes the excitonic resonance energy. At energies higher than E_0 , the absorption coefficient determined with this standard method is in good agreement with the one determined by heterodyne interference spectroscopy at 6.5 and 160 K.

In Fig. 7(d), only the absorption coefficient calculated from heterodyne interference spectroscopy at 160 K exhibits two peaks on the low-energy side of E_0 . We designated these peaks A and B. The temperature dependence of these peaks is different from that of E_0 . As shown in Fig. 7(e), E_0 shifts to a lower energy as the temperature decreases. Unlike GaAs, the lattice constant of lead-halide perovskites decreases with decreasing temperature, which enhances the overlap of the antibonding orbitals that constitute the top of the valence band, specifically, the Pb(6s) and Br(5p) orbitals. Consequently, the energy at the top of the valence band increases and E_0 shifts to lower energies with decreasing temperature.^{35,36} On the other hand, peaks A and B shift to higher energies with decreasing temperature, as shown in Fig. 7(e).

Since the temperature dependence of the energies of peaks A and B differs from that of E_0 , we can attribute the origins of these peaks to an indirect transition caused by the Rashba spin-splitting band.¹⁵ The Rashba effect arises from strong spin-orbit interactions and spatial inversion symmetry breaking.^{37–39} Both the valence and conduction bands split into two spin-polarized bands, but the conduction band split is larger. In MAPbBr₃ single crystals, local electric fields are generated by the MA cation and thermal fluctuations in the Pb–Br cage mode, which break the spatial inversion symmetry.^{38,40} The thermal fluctuations in the MA cation and Pb–Br cage mode decrease with temperature and this reduces the band-splitting width, and the energies of peaks approach E_g . Since the energy difference between the peaks is twice the LO phonon energy of a MAPbBr₃ single crystal (20.1 meV),⁴¹ peak A corresponds to the phonon emission (Stokes) and peak B corresponds to absorption (anti-Stokes) processes.

The conventional photocurrent measurements did not reveal peak A or B, but the heterodyne interference spectroscopy did. As mentioned above, these peaks are assumed to be indirect transitions to the Rashba spin-splitting band. Typically, the shape of the absorption at the band edge in indirect transitions, similarly to the band edges of Si and Ge, gradually rises and does not have a peak structure. Therefore, conventional photocurrent measurements did not show a peak structure in the band tail. Peaks A and B can be attributed to quantum interference effects on ultra-short timescales (tens of femtoseconds) due to the heterodyne interference spectroscopy, and the dynamical Rashba effect occurs on a hundred-femtosecond time scale, i.e., the time scale of the thermal fluctuations of the MA cation and Pb–Br cage mode. Further research should be conducted on the unresolved aspects of this mechanism.

29 June 2024 17:17:24

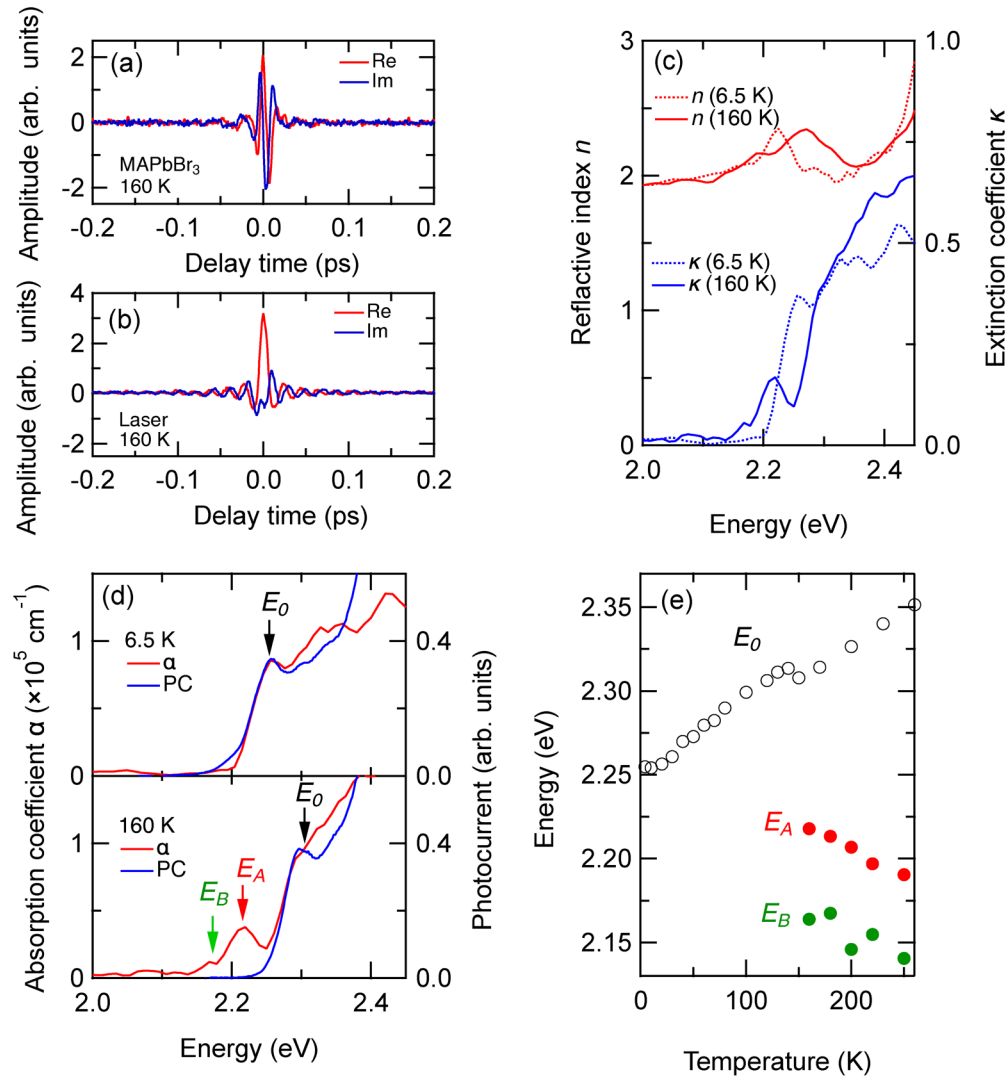


FIG. 7. (a) Interferograms of (a) an MAPbBr₃ single crystal at 6.5 and 160 K and (b) an excitation-pulse pair. (c) Reflective index and extinction coefficient calculated from dielectric susceptibility at 6.5 and 160 K. (d) Absorption coefficient obtained by interference spectroscopy and experimentally obtained photocurrent. (e) Temperature dependences of excitonic resonance energy (E_0 ; black open circles) and energy of peak A (E_A ; red circles) and B (E_B ; green circles).

IV. CONCLUSIONS

We developed interferometric spectroscopy of photocurrents (both homodyne and heterodyne spectroscopy) for characterizing solar-cell materials. To demonstrate its usefulness, we performed experiments on three different photocurrent-converting materials: GaAs, quantum dots (QDs), and lead-halide perovskites.

Photocurrent beat spectroscopy using the homodyne interference technique is a powerful tool for determining multiple photocurrent generation sources. We used it to determine the sources in GaAs at temperatures ranging from room temperature down to cryogenic temperatures. The temperature-dependent photocurrent

spectra revealed how photocurrent sources are related to the ionization process of acceptor levels. A comparison of the photocurrent and photoluminescence spectra indicated that radiative recombination is suppressed at the ionized level, while the ionized level strongly contributes to the photocurrent. Additionally, we demonstrated that heterodyne interference spectroscopy is a useful way to obtain broadband spectra of the reflective index, extinction coefficient, absorption, and reflective properties of GaAs. In heterodyne interference spectroscopy, the absolute value of the horizontal axis (frequency) of the spectrum is determined using an integral transformation of the real and imaginary parts of the interferogram. This method is robust to fluctuations of the interferometer because

a portion of the interference signal is used as a reference signal for lock-in detection. To improve the efficiency of solar cells, it is important to characterize the deeper trap and defect states. By tuning the wavelength of the lasers to their energies, it should be possible to measure the electro-optical parameters of the deeper trap and defect states.

These techniques are also valuable for analyzing new solar-cell materials. Photocurrent interference spectroscopy of PbS QD solar cells revealed a cooperative enhancement effect in a QD ensemble. Since multiexcitons arising from the inter-QD coupling enhance photocurrent signals with high oscillation frequencies, the observed cooperative enhancement provides deep insights for improving the power conversion efficiency of solar cells. Additionally, heterodyne interference spectroscopy of photocurrent in bulk lead-halide perovskites detected a signal originating from the Rashba effect at the low-energy side of the exciton resonance energy. Heterodyne interference spectroscopy is based on quantum interference effects that occur within tens of femtoseconds. Therefore, it can be used to observe novel phenomena, such as Rashba effects, that do not appear in ordinary spectroscopic measurements.

As shown by the above examples, interference spectroscopy of photocurrent is a sensitive means of evaluating localized levels within semiconductor materials, which are difficult to measure with conventional spectroscopy. The ability to identify localized levels within solar-cell materials shows potential for improving the quality of photovoltaic devices. Additionally, interference spectroscopy of photocurrent reveals interesting phenomena, such as the cooperative effect between QDs and the Rashba effect. Such discoveries could potentially inform the development of novel functionalities in solar cells.

Our methods entail measuring the interference signal of photocurrent induced by optical pulse irradiation. This approach can be adapted to evaluate the dynamic response of photocarriers. Similar to pump-probe spectroscopy, using an excitation pulse as a pre-pulse and scanning the delay time could improve our understanding of the dynamic process involved in photo-current conversion. These insights will be crucial for investigating novel solar-cell materials and new device designs.

In summary, interference spectroscopy of photocurrent is capable of measuring localized levels within semiconductor materials with high sensitivity and accuracy and will be instrumental in advancing the development of optical devices.

ACKNOWLEDGMENTS

This work was supported by the International Collaborative Research Program of Institute for Chemical Research, Kyoto University (Grant No. 2023-22). Part of this work was supported by the JSPS KAKENHI grant (No. JP19H05465; Y.K. and H.T.), (No. JP21K03429; Y.O.), and (Nos. JP23K17877 and JP23K23258; H.T.). Y.O. would like to thank T. Tomizuka for useful discussions about the heterodyne interference spectroscopy of GaAs.

AUTHOR DECLARATIONS

Conflict of Interest

The authors have no conflicts to disclose.

Author Contributions

Yoshihiro Ogawa: Conceptualization (equal); Data curation (equal); Formal analysis (equal); Funding acquisition (equal); Investigation (equal); Methodology (equal); Project administration (equal); Validation (equal); Visualization (equal); Writing – original draft (equal); Writing – review & editing (equal). **Hirokazu Tahara:** Conceptualization (equal); Data curation (equal); Formal analysis (equal); Funding acquisition (equal); Investigation (equal); Methodology (equal); Project administration (equal); Validation (equal); Visualization (equal); Writing – original draft (equal); Writing – review & editing (equal). **Yoshihiko Kanemitsu:** Conceptualization (equal); Funding acquisition (equal); Project administration (equal); Supervision (equal); Validation (equal); Writing – review & editing (equal).

DATA AVAILABILITY

The data that support the findings of this study are available from the corresponding authors upon reasonable request.

REFERENCES

- K. Seeger, *Semiconductor Physics*, 9th ed. (Springer, Berlin, 2004).
- R. H. Bube, *Photoconductivity of Solids* (John Wiley & Sons, New York, 1960).
- A. Rose, *Concepts in Photoconductivity and Allied Problems* (Krieger, New York, 1978).
- Y. Marfaing, “Photoconductivity, photoelectric effects,” in *Handbook on Semiconductors*, edited by T. S. Moss and M. Balkanski (North-Holland, Amsterdam, 1980), Vol. 2, pp. 417–495.
- Y. Yamada and Y. Kanemitsu, *Appl. Phys. Lett.* **101**, 133907 (2012).
- Y. Yamada, T. Nakamura, M. Endo, A. Wakamiya, and Y. Kanemitsu, *Appl. Phys. Express* **7**, 032302 (2014).
- L. Q. Phuong, Y. Nakaike, A. Wakamiya, and Y. Kanemitsu, *J. Phys. Chem. Lett.* **7**, 4905 (2016).
- M. Born and E. Wolf, *Principles of Optics*, 7th ed. (Cambridge University Press, Cambridge, 2001).
- Y. Yamada, D. M. Tex, I. Kamiya, and Y. Kanemitsu, *Appl. Phys. Lett.* **107**, 013905 (2015).
- J. Gao, A. F. Fidler, and V. I. Klimov, *Nat. Commun.* **6**, 8185 (2015).
- E. Kobiyama, H. Tahara, M. Saruyama, R. Sato, T. Teranishi, and Y. Kanemitsu, *Appl. Phys. Lett.* **122**, 252106 (2023).
- M. Vanecek and A. Poruba, *Appl. Phys. Lett.* **80**, 719 (2002).
- H. Tahara, M. Sakamoto, T. Teranishi, and Y. Kanemitsu, *Phys. Rev. B* **104**, L241405 (2021).
- H. Tahara, M. Sakamoto, T. Teranishi, and Y. Kanemitsu, *Nat. Nanotechnol.* **19** (2024).
- Y. Ogawa, H. Tahara, N. Igarashi, Y. Yamada, and Y. Kanemitsu, *Phys. Rev. B* **103**, L081210 (2021).
- H. Tahara and Y. Kanemitsu, *Phys. Rev. B* **90**, 245203 (2014).
- D. J. Ashen, P. J. Dean, D. T. J. Hurle, J. B. Mullin, A. M. White, and P. D. Greene, *J. Phys. Chem. Solids* **36**, 1041 (1975).
- H. Tahara and Y. Kanemitsu, *Appl. Phys. Express* **9**, 032403 (2016).
- H. Tahara, M. Endo, A. Wakamiya, and Y. Kanemitsu, *J. Phys. Chem. C* **120**, 5347 (2016).
- P. F. Tekavec, T. R. Dyke, and A. H. Marcus, *J. Chem. Phys.* **125**, 194303 (2006).
- K. Papatryfonos, T. Angelova, A. Brimont, B. Reid, S. Guldin, P. R. Smith, M. Tang, K. Li, A. J. Seeds, H. Liu, and D. R. Selviah, *AIP Adv.* **11**, 025327 (2021).
- H. Haug and S. W. Koch, *Quantum Theory of the Optical and Electronic Properties of Semiconductors*, 5th ed. (World Scientific, Singapore, 2009).
- P. Y. Yu and M. Cardona, *Fundamentals of Semiconductors*, 4th ed. (Springer, Berlin, 2010).

29 June 2024 17:17:24

- ²⁴M. D. Sturge, *Phys. Rev.* **127**, 768 (1962).
- ²⁵R. D. Schaller and V. I. Klimov, *Phys. Rev. Lett.* **92**, 186601 (2004).
- ²⁶R. J. Ellingson, M. C. Beard, J. C. Johnson, P. Yu, O. I. Micic, A. J. Nozik, A. Shabaev, and A. L. Efros, *Nano Lett.* **5**, 865 (2005).
- ²⁷A. Shabaev, A. L. Efros, and A. J. Nozik, *Nano Lett.* **6**, 2856 (2006).
- ²⁸O. E. Semonin, J. M. Luther, S. Choi, H.-Y. Chen, J. Gao, A. J. Nozik, and M. C. Beard, *Science* **334**, 1530 (2011).
- ²⁹A. Shabaev, C. S. Hellberg, and A. L. Efros, *Acc. Chem. Res.* **46**, 1242 (2013).
- ³⁰H. Tahara and Y. Kanemitsu, *Adv. Quantum Technol.* **3**, 1900098 (2020).
- ³¹H. Tahara, M. Sakamoto, T. Teranishi, and Y. Kanemitsu, *Phys. Rev. Lett.* **119**, 247401 (2017).
- ³²H. Tahara, M. Sakamoto, T. Teranishi, and Y. Kanemitsu, *Nat. Commun.* **9**, 3179 (2018).
- ³³M. I. Saidaminov, A. L. Abdelhady, B. Murali, E. Alarousu, V. M. Burlakov, W. Peng, I. Dursun, L. Wang, Y. He, G. Maculan, A. Goriely, T. Wu, O. F. Mohammed, and O. M. Bakr, *Nat. Commun.* **6**, 7586 (2015).
- ³⁴A. M. A. Leguy, P. Azarhoosh, M. I. Alonso, M. Campoy-Quiles, O. J. Weber, J. Yao, D. Bryant, M. T. Weller, J. Nelson, A. Walsh, M. van Schilfgaarde, and P. R. F. Barnes, *Nanoscale* **8**, 6317 (2016).
- ³⁵B. J. Foley, D. L. Marlowe, K. Sun, W. A. Saidi, L. Scudiero, M. C. Gupta, and J. J. Choi, *Appl. Phys. Lett.* **106**, 243904 (2015).
- ³⁶L.-Y. Huang and W. R. L. Lambrecht, *Phys. Rev. B* **88**, 165203 (2013).
- ³⁷F. Zheng, L. Z. Tan, S. Liu, and A. M. Rappe, *Nano Lett.* **15**, 7794 (2015).
- ³⁸E. Mosconi, T. Etienne, and F. De Angelis, *J. Phys. Chem. Lett.* **8**, 2247 (2017).
- ³⁹T. Etienne, E. Mosconi, and F. De Angelis, *J. Phys. Chem. Lett.* **7**, 1638 (2016).
- ⁴⁰O. Yaffe, Y. Guo, L. Z. Tan, D. A. Egger, T. Hull, C. C. Stoumpos, F. Zheng, T. F. Heinz, L. Kronik, M. G. Kanatzidis, J. S. Owen, A. M. Rappe, M. A. Pimenta, and L. E. Brus, *Phys. Rev. Lett.* **118**, 136001 (2017).
- ⁴¹M. Nagai, T. Tomioka, M. Ashida, M. Hoyano, R. Akashi, Y. Yamada, T. Aharen, and Y. Kanemitsu, *Phys. Rev. Lett.* **121**, 145506 (2018).